JOURNAL OF MATERIALS SCIENCE 27 (1992) 68–76

Crack deflection by rod-shaped inclusions

YIH-CHERNG CHIANG
Center for Composite Materials and Department of Mechanical Engineering, University of Delaware, Newark, DE 19716, USA

This paper presents a model for crack deflection around rod-shaped inclusions. In this analysis both a stress intensity factor approach and a crack surface area approximation are used. The local stress intensity factors of a deflected crack along two adjacent rod-shaped inclusions are derived first. Then, the path of advancement of the deflected crack front along the inclusions can be determined. Knowledge of the crack path provides the basis for evaluating the deflection-induced reduction in strain energy release rate as well as the basis for calculating the deflected crack surface area. The analytical predictions are compared with the theoretical results of Faber and Evans and the differences between these two analyses are discussed.

1. Introduction

The purpose of this paper is to study the crack deflection processes. Crack deflection is an effective toughening mechanism in polycrystalline ceramics [1] and in brittle matrices containing second-phase inclusions [2–6].

Crack deflection may arise from either residual stresses in an inhomogeneous material or weak inclusion–matrix interfaces. The non-planar crack due to deflection results in an enhanced toughness. Experimental observations of the deflection of microcracks through grain boundaries in polycrystalline solids and a conventional fracture mechanics analysis were carried out by Gell and Smith [1]. Crack deflection was also identified as the major toughening mechanisms for Si_3N_4 with rod-shaped β-phase [7, 8] and whisker-reinforced glass and ceramic matrix composites [4–6]. More recently, the deflection of cracks around second-phase inclusions was analysed by Faber and Evans [2, 3]. In their pioneering analysis the toughness increases due to crack deflection are related to the volume fraction, morphology and aspect ratio of inclusions. However, their analysis has two limitations. First, the validity of the local stress intensity factor expressions of a deflected crack is uncertain. Second, it was assumed that maximum toughness due to crack deflection is achieved when the crack front reaches the end-points of the two neighbouring rod-shaped inclusions. This would require the crack front to assume certain configurations which are sometimes not energetically feasible. For the general crack-path problem, the energetically favoured crack front position is the one that maximizes the strain energy release rate [9]. Consequently, in the following analysis we identify the path of crack extension which satisfies this requirement.

In this paper, a comprehensive treatment of the crack deflection processes for rod-shaped inclusions based upon a modification to the work of Faber and Evans [2] is given. First, the three-dimensional stress intensity factors of a deflected crack along two adjacent rod-shaped inclusions are derived. Then, the crack deflection profile along the rod-shaped inclusions is identified by the maximum strain energy release rate approach. The crack front position responsible for maximum toughening is discussed. In the present analysis the second-phase inclusions are modelled as having the same elastic properties as the matrix. Therefore, the elastic interaction between the matrix and inclusions can be neglected.

2. Analysis of crack deflection

2.1. General considerations

Fig. 1 depicts a crack of length c deflected by an angle θ. This deflection results in a "tilted" crack. It can be viewed as due to a rotation of angle θ with the rotational axis parallel to the z-axis and passing through point O′. The x' axis lies in the deflected crack plane. Fig. 2 illustrates a "twisted" crack which is achieved through a rotation of the crack about the x-axis for an angle ϕ. The x (x') axis also lies in the deflected crack plane. Under an applied tensile load in the y direction the tilted crack gives rise to both Mode I (opening) and Mode II (shearing) fractures. Similarly, the twisted crack induces both Mode I and Mode III (tearing) fractures [9].

The enhancement in fracture toughness due to crack deflection can be evaluated based upon the knowledge of the stress intensity factors K_I, K_{II} and K_{III}. The extension of the crack is then governed by the strain energy release rate, G, along its deflected trajectory

$$G = \frac{K_I^2(1 - \nu^2) + K_{II}^2(1 - \nu^2) + K_{III}^2(1 + \nu)}{E} \quad (1)$$

Here, E and ν are, respectively, the Young's modulus and Poisson's ratio of the material.

The strain energy release rate due to crack deflection is evaluated from the stress intensity factors of the deflected crack front. Then, the critical strain energy release rate, G_c, is obtained by considering the

0022–2461/92 $03.00 + .12

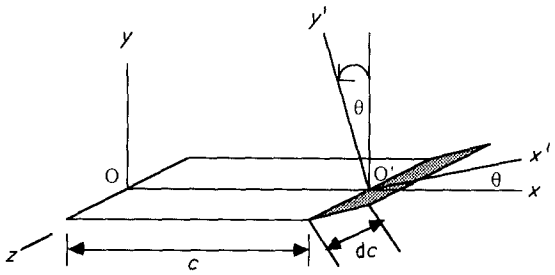

Figure 1 Tilted crack configuration depicting a crack of length c deflected by an angle θ.

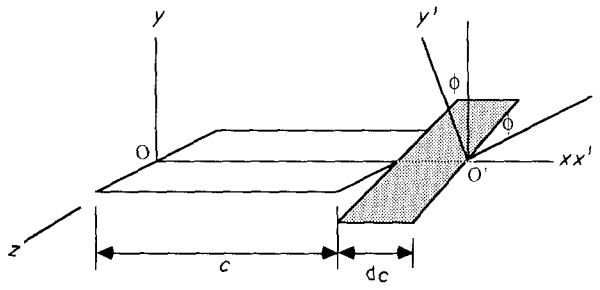

Figure 2 Twisted crack configuration which is achieved through a rotation of the original crack about the x-axis for an angle ϕ. Both x and x' axes lie in the deflected crack surface.

ratio of the strain energy release rates of the undeflected (G^m) and deflected ($\langle G \rangle$) cracks [2]

$$G_c = \frac{G^m}{\langle G \rangle} G_c^m \tag{2}$$

where G_c^m is the critical strain energy release rate of an undeflected crack, and $\langle G \rangle$ is the average value for all the possible deflected crack configurations.

2.2. Stress intensity factor approach

2.2.1. Local stress intensity factors of a deflected crack

The stress intensity factor expressions of a crack front propagating along two neighbouring rod-shaped inclusions are more complex than the cases of Figs 1 and 2, because the deflected crack plane exhibits concomitant tilting and twisting. This is a three-dimensional problem and the deflected crack front gives rise to all three modes of fracture (I, II and III). The exact three-dimensional stress intensity factor solution is difficult to obtain. The approach of the "transformed stress-intensity factor" of Gell and Smith [1], Lawn and Wilshaw [9] and Faber and Evans [2] is adopted in the present analysis. The stress intensity factors of a deflected crack under an applied tensile stress σ_y, as shown schematically in Fig. 3, can be expressed as

$$K_I^d = f_1(\theta, \phi, \psi) K_I \tag{3a}$$

$$K_{II}^d = f_2(\theta, \phi, \psi) K_I \tag{3b}$$

$$K_{III}^d = f_3(\theta, \phi, \psi) K_I \tag{3c}$$

where the angular functions, f_1, f_2 and f_3, associated with the tilt angle θ, twist angle ϕ and bias angle ψ (Fig. 3) are determined by resolving the stress components of a tilted crack plane into the deflected crack plane (see Appendix); K_I is the stress intensity fracture of the main crack. The expressions for $f_1(\theta, \phi, \psi)$, $f_2(\theta, \phi, \psi)$ and $f_3(\theta, \phi, \psi)$ are

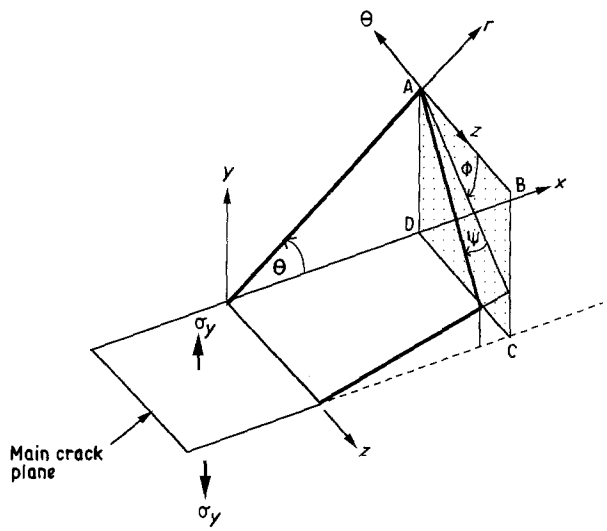

Figure 3 Schematic view of a deflected crack front with tilt angle θ, twist angle ϕ and bias angle ψ.

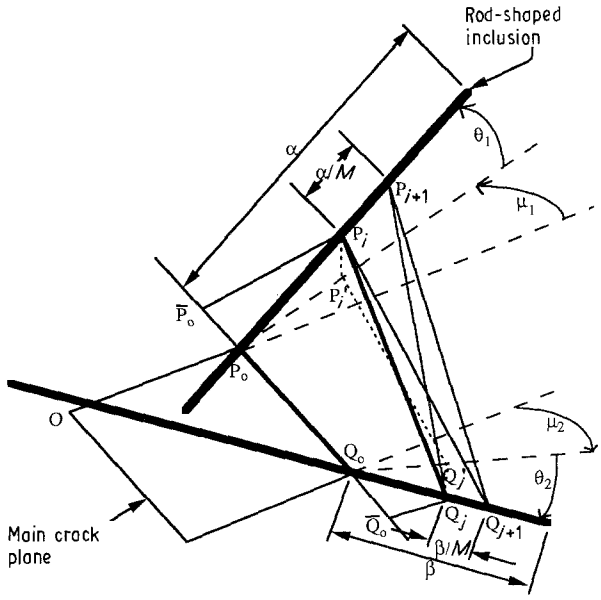

Figure 4 Schematic view of crack deflection by two neighbouring rod-shaped inclusions.

$$f_1(\theta, \phi, \psi) = \cos^3(\theta/2)[2\nu \sin^2\phi + \cos^2\phi] \tag{4a}$$

$$f_2(\theta, \phi, \psi) = \sin(\theta/2)\cos^2(\theta/2)\cos\phi\cos\psi - (1 - 2\nu)\cos^3(\theta/2)\sin\phi\cos\phi\sin\psi \tag{4b}$$

$$f_3(\theta, \phi, \psi) = -\sin(\theta/2)\cos^2(\theta/2)\cos\phi\sin\psi - (1 - 2\nu)\cos^3(\theta/2)\sin\phi\cos\phi\cos\psi \tag{4c}$$

where ν is the Poisson's ratio of the matrix material.

Faber and Evans [2] defined two types of crack deflection: same-sign deflection for $\text{sign}(\theta_1) = \text{sign}(\theta_2)$ (Fig. 3), and opposite-sign deflection for

$\text{sign}(\theta_1) = -\text{sign}(\theta_2)$ (Fig. 4). In Faber and Evans [2], the modelling of same-sign deflection is performed by simplifying the deflection to a pure tilt crack with an average tilt angle of $(\theta_1 + \theta_2)/2$. As a result, the effects of the twist (ϕ) and bias (ψ) crack front orientation on the strain energy release rate are ignored. Also, the stress component $\tau_{r\theta}$ (see Appendix) which is responsible for Mode II fracture has been included in the present analysis; this is essential in the consideration of crack deflection and is missing in the expressions of the stress intensity factors of an opposite-sign crack in the analysis of Faber and Evans. Furthermore, using the comprehensive stress intensity factor expressions of Equations 4, the strain energy release rates of any general configurations of rod-shaped inclusions can be evaluated. Thus, it is unnecessary to treat the same-sign and opposite-sign deflections separately, as in Faber and Evans [2].

2.2.2. Crack deflection model

For the purpose of illustration, we consider the interaction of a crack front (line P_0Q_0 in Fig. 4) with two adjacent rod-shaped inclusions oriented at angles θ_1, θ_2, μ_1 and μ_2 with respect to the main crack plane. In order to define the morphology of the deflected crack surface in Fig. 4, the two inclusion segments protruding from the main crack plane are divided into M segments. Let α and β denote the lengths of the two segments; the divisions on the two segments are of lengths α/M and β/M. Furthermore, knowing the angular positions θ_1 and μ_1, and θ_2 and μ_2 for the inclusions, the angles λ_1 and λ_2 of Fig. 4 can be readily written as

$$\lambda_1 = \tan^{-1}(\tan\theta_1/\cos\mu_1) \quad (5a)$$

$$\lambda_2 = \tan^{-1}(\tan\theta_2/\cos\mu_2) \quad (5b)$$

A general crack front is denoted by P_iQ_j. For clarity, the geometric configuration of the deflected crack is recapitulated in Fig. 5. The twist angle ϕ_{ij} and bias angle ψ_{ij} are indicated, and their expressions are, respectively,

$$\phi_{ij} = \tan^{-1}\left[\left(\frac{i}{M}\alpha\sin\theta_1 - \frac{j}{M}\beta\sin\theta_2\right)\Big/\left(P_0Q_0 + \frac{i}{M}\alpha\cos\theta_1\sin\mu_1 - \frac{j}{M}\beta\cos\theta_2\sin\mu_2\right)\right] \quad (6)$$

$$\psi_{ij} = \sin^{-1}\left[\left(\frac{i}{M}\alpha\cos\theta_1\cos\mu_1 - \frac{j}{M}\beta\cos\theta_2\cos\mu_2\right)\Big/(P_iQ_j)\right] \quad (7)$$

where the length of crack front, P_iQ_j, is given by

$$P_iQ_j = \left[(\Delta'_{ij})^2 + \left(\frac{i}{M}\alpha\sin\theta_1 - \frac{j}{M}\beta\sin\theta_2\right)^2\right]^{1/2} \quad (8)$$

Δ'_{ij} in Equation 8 indicates the projected length $P'_iQ'_j$ (Fig. 4) and it is expressed as

$$\Delta'_{ij} = \left[\left(\Delta + \frac{i}{M}\alpha\cos\theta_1\sin\mu_1 - \frac{j}{M}\beta\cos\theta_2\sin\mu_2\right)^2 + \left(\frac{i}{M}\alpha\cos\theta_1\cos\mu_1 - \frac{j}{M}\beta\cos\theta_2\cos\mu_2\right)^2\right]^{1/2} \quad (9)$$

where Δ is the length of P_0Q_0.

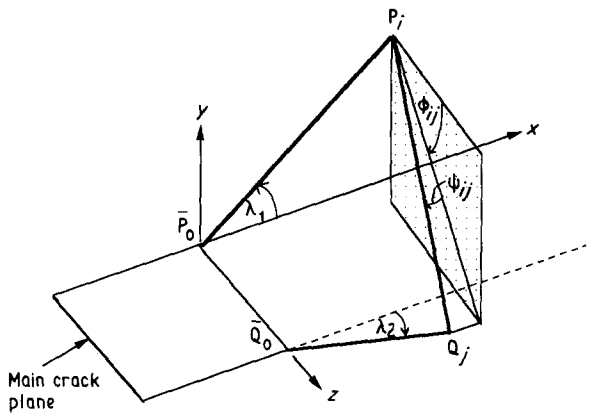

Figure 5 Another representation of the crack front P_iQ_j in Fig. 4.

In the following analysis, Δ is chosen as the centre-to-centre distance between two neighbouring randomly positioned rod-shaped inclusions. An approximation of this parameter is given by Bansal and Ardell [10] for the nearest-neighbour spacing between two cylinders of finite length in a random array:

$$\frac{\Delta}{r} = \frac{e^{4V_f}}{V_f^{1/2}}\int_{4V_f}^{\infty} x^{1/2}\exp(-x)\,dx \quad (10)$$

where r is the inclusion radius and V_f is the inclusion volume fraction.

The strain energy release rate, $\langle G\rangle$, of the crack front P_iQ_j, normalized with respect to that of the undeflected crack, G^m, is given as

$$\frac{\langle G\rangle_{P_iQ_j}}{G_m} = \frac{\eta_{ij}}{\lambda_1 - \lambda_2}\int_{\lambda_2}^{\lambda_1}\left\{[f_1(\lambda,\phi_{ij},\psi_{ij})]^2 + [f_2(\lambda,\phi_{ij},\psi_{ij})]^2 + \frac{1+\nu}{1-\nu^2}[f_3(\lambda,\phi_{ij},\psi_{ij})]^2\right\}d\lambda \quad (11)$$

where η_{ij} is the ratio of the undeflected to deflected crack front length, which can be expressed as

$$\eta_{ij} = \left(\Delta + \frac{i}{M}\alpha\cos\theta_1\sin\mu_1 - \frac{j}{M}\beta\cos\theta_2\sin\mu_2\right)\Big/\left[(\Delta'_{ij})^2 + \left(\frac{i}{M}\alpha\sin\theta_1 - \frac{j}{M}\beta\sin\theta_2\right)^2\right]^{1/2} \quad (12)$$

The integral in Equation 11 is due to the angle, λ, varying from λ_1 to λ_2.

The propagation of the crack front from its initial location of P_0Q_0 in Fig. 4 is discussed in the following. Although crack propagation along the inclusions is believed to be a continuous process, we focus on the crack front locations at $P_0, P_1, \ldots, P_i, \ldots, P_M$ along the inclusion of length α, and the locations at $Q_0, Q_1, \ldots, Q_j, \ldots, Q_M$ along the inclusion of length β, for the convenience of numerical calculations. Now

consider an instantaneous location of the crack front at P_iQ_j. The subsequent crack front location, according to the divisions made on the inclusion segments, could be P_iQ_{j+1}, $P_{i+1}Q_j$ or $P_{i+1}Q_{j+1}$. The strain energy release rates correspoding to these three paths of crack extension are calculated and the new crack front location associated with the maximum strain energy release rate is identified. If, for instance, the crack front assumes the new position of P_iQ_{j+1}, the calculation process for G is repeated for the locations of P_iQ_{j+2}, $P_{i+1}Q_{j+1}$ and $P_{i+1}Q_{j+2}$. The process of calculations will terminate when either one of the following two situations is attained. First, this process continues until the crack front reaches the end of one of the inclusions. The further extension of the deflected crack occurs in the matrix and the crack path becomes unknown. In this case the maximum toughening is accomplished by the crack front position that has the smallest strain energy release rate among all instantaneous crack front positions. Second, under some crack configurations the strain energy release rate of the crack front will approach to zero (i.e. the infinite critical energy release rate). Further movement along the inclusions will cause the unreasonable result of negative strain energy release rate. For such crack configurations the strain energy release rate of the crack front which is responsible for the maximum toughening approaches to zero.

By integrating over all the possible relative positions of the two rod-shaped inclusions of identical length, L, (i.e. lengths α and β, and orientation angles θ_1, θ_2, μ_1 and μ_2), the average strain energy release rate is expressed in the general form as

$$\frac{\langle G\rangle}{G^m} = \frac{2}{L^2\pi^4}\int_0^L\int_0^L\int_{-\pi/2}^{\pi/2}\int_{-\pi/2}^{\pi/2}\int_{-\pi/2}^{\pi/2}\int_0^{\pi/2}\frac{\eta_{IJ}}{\lambda_1-\lambda_2}\times\int_{\lambda_2}^{\lambda_1}\left\{[f_1(\lambda,\phi_{IJ},\psi_{IJ})]^2+[f_2(\lambda,\phi_{IJ},\psi_{IJ})]^2+\frac{1+\nu}{1-\nu^2}[f_3(\lambda,\phi_{IJ},\psi_{IJ})]^2\right\}\times d\lambda\,d\theta_1\,d\theta_2\,d\mu_1\,d\mu_2\,d\alpha\,d\beta \quad (13)$$

where the subscript IJ represents the crack front position that achieves the maximum toughening for each crack configuration. In the numerical calculation, each of the parameters α, β, θ_1, θ_2, μ_1 and μ_2 is subdivided into many increments when considering all the possible inclusion configurations. Finally, the critical strain energy release rate, G_c, is obtained from Equation 2.

2.3. Crack surface area approximation

The surface area of a deflected crack, S^d, relative to that of an undeflected crack, S^m, can be regarded as an estimate of increment in critical strain energy release rate. In the analysis of Faber and Evans [2], the "resultant toughness" from the crack surface area approximation is given by

$$\frac{G_c}{G_c^m} = \frac{S^d}{S^m} = \frac{2}{\pi\Delta}\int_0^{\pi/2}\left[\left(\frac{\Delta}{2}\right)^2+\left(\frac{H}{2r}r\sin\theta\right)^2\right]^{1/2}d\theta + \frac{1}{\pi}\int_0^{\pi/2}\sec\theta\,d\theta \quad (14)$$

where r and H are the radius and length of a rod-shaped inclusion, respectively. This simple approximation of crack surface area cannot reflect the surface morphology induced by deflection around inclusions. A close estimation of crack surface area is presented in the following.

The deflected crack surface area defined by two adjacent rod-shaped inclusions can be calculated by summing the triangular areas identified by the crack path (section 2.2.2). Considering the case of a twisted crack, for instance, the lengths of P_iQ_j and $P_i'Q_j'$ from the triangle $P_iQ_jQ_{j+1}$ (Fig. 6) are, respectively, given by Equations 8 and 9. Similarly, expressions for P_iQ_{j+1} and $P_i'Q_{j+1}'$ can be obtained. The area of the triangle $P_iQ_jQ_{j+1}$ is given by

$$P_iQ_jQ_{j+1} = \left[S_{P_iQ_jQ_{j+1}}\left(S_{P_iQ_jQ_{j+1}}-\frac{\beta}{M}\right)(S_{P_iQ_jQ_{j+1}}-P_iQ_j)(S_{P_iQ_jQ_{j+1}}-P_iQ_{j+1})\right]^{1/2} \quad (15)$$

where

$$S_{P_iQ_jQ_{j+1}} = \frac{1}{2}\left(\frac{\beta}{M}+P_iQ_j+P_iQ_{j+1}\right) \quad (16)$$

The projected area of the deflected crack on the undeflected crack plane is

$$P_i'Q_j'Q_{j+1}' = \left[S'_{P_iQ_jQ_{j+1}}\left(S'_{P_iQ_jQ_{j+1}}-\frac{\beta\cos\theta_2}{M}\right)\times(S'_{P_iQ_jQ_{j+1}}-P_i'Q_j')(S'_{P_iQ_jQ_{j+1}}-P_i'Q_{j+1}')\right]^{1/2} \quad (17)$$

where

$$S'_{P_iQ_jQ_{j+1}} = \frac{1}{2}\left(\frac{\beta\cos\theta_2}{M}+P_i'Q_j'+P_i'Q_{j+1}'\right) \quad (18)$$

Integrating over all possible inclusion configurations,

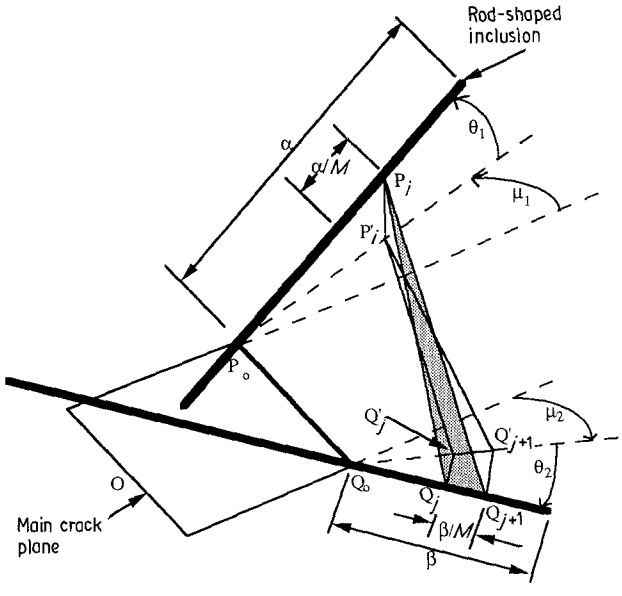

Figure 6 A crack surface area created by the advancement of crack front from P_iQ_j to P_iQ_{j+1}.

the relative surface areas can be written as

$$\frac{S^d}{S^m} = \frac{2}{L^2\pi^4}\int_0^L\int_0^L\int_{-\pi/2}^{\pi/2}\int_{-\pi/2}^{\pi/2}\int_{-\pi/2}^{\pi/2}\int_0^{\pi/2} \times \sum_{n=1} \frac{\{S[S-(\beta/M)](S-P_iQ_j)(S-P_iQ_{j+1})\}^{1/2}}{\{S'[S'-(\beta\cos\theta_2/M)](S'-P'_jQ'_j)(S'-P'_iQ'_{j+1})\}^{1/2}} d\theta_1\, d\theta_2\, d\mu_1\, d\mu_2\, d\alpha\, d\beta \quad (19)$$

where S and S' are the simplified notations for $S_{P_iQ_jQ_{j+1}}$ and $S'_{P_iQ_jQ_{j+1}}$, respectively. Then the relative critical strain energy release rate, G_c/G_c^m, by the crack surface area approximation is obtained from S^d/S^m by using Equation 14.

3. Numerical results and discussions

In the numerical integrations for fracture toughness and crack surface area, a step-wise calculation is performed at incremental values of α, β, θ_1, θ_2, μ_1 and μ_2. Furthermore, at each step of calculation, M subdivisions are made along the inclusions to determine the paths of the crack front movement. The sensitivity of the end results to the subdivisions, M, has been examined. Fig. 7 depicts the variation of fracture toughness (G_c/G_c^m) predictions with the number of subdivisions (M). The calculation is performed for the inclusion volume fraction $V_f = 0.2$ and aspect ratio $R = 12$. The fracture toughness values obtained from the stress intensity factor approach decrease as M increases, and approach the asymptotic value for $M > 100$.

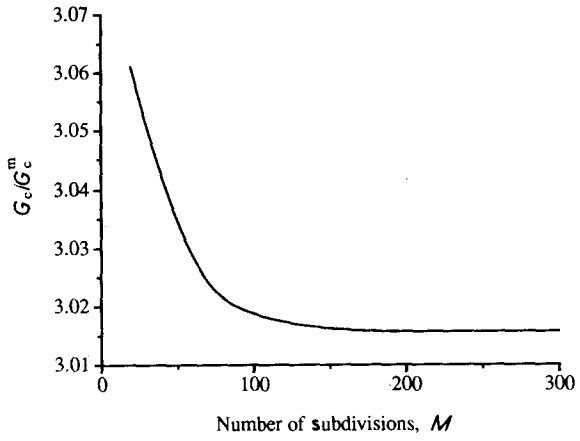

Figure 7 Relative critical strain energy release rate versus number of subdivisions at inclusion volume fraction $V_f = 0.2$ and aspect ratio $R = 12$.

The profiles of crack front positions along two adjacent rod-shaped inclusions and the corresponding relative strain energy release rates, G/G^m, are illustrated in Figs 8, 9 and 10 for three specific cases. The solid line segments between the two inclusions indicate schematically the instantaneous crack front positions identified by the present approach. At the initial stage of deflection, the decrease in strain energy release rate is mainly due to the tilting of the crack front. Subsequently, the dependence of toughening on the twisting of the crack front and the increase of the crack front length becomes significant.

Figs 8–10 indicate another major difference in the crack paths of Faber and Evans [2] and the present approach. Faber and Evans assumed that the crack

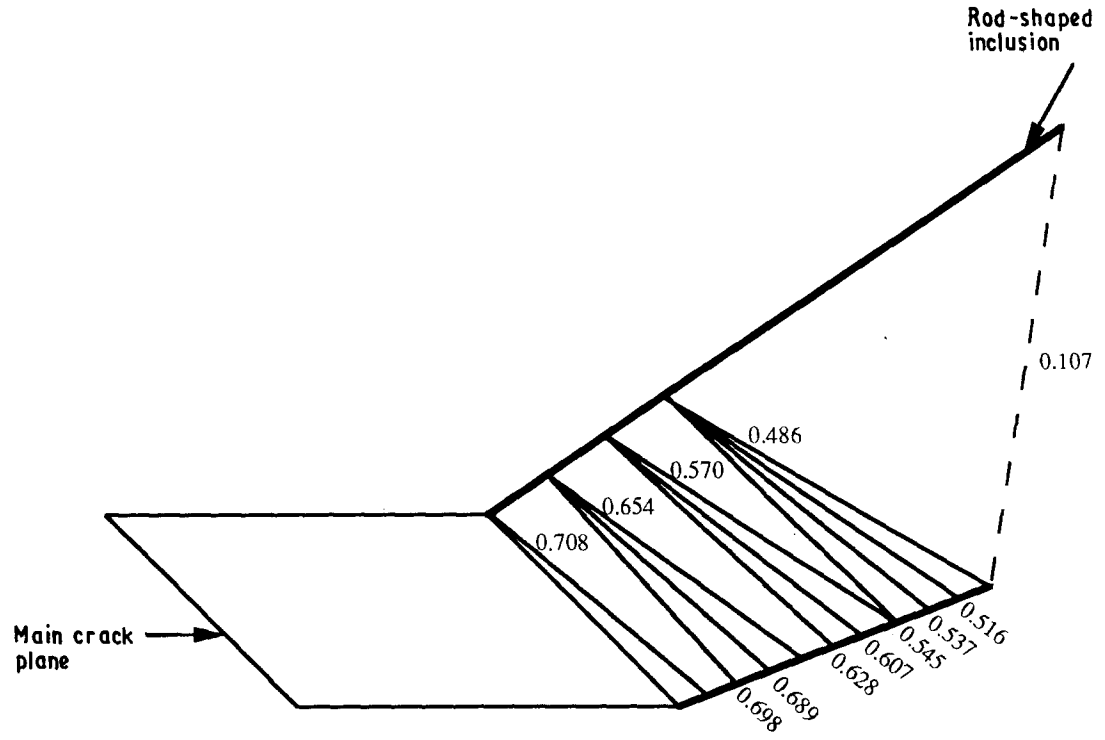

Figure 8 Schematic diagram of the crack path between two adjacent inclusions with values of the relative strain energy release rates, G/G^m, corresponding to these crack front positions for the case of $V_f = 0.2$, $R = 6$, $\alpha = L$, $\beta = 0.5L$, $\mu_1 = 0$, $\mu_2 = 0$, $\theta_1 = \pi/3$, $\theta_2 = \pi/6$. The dashed line linking two inclusion ends is the crack front position used to calculate the strain energy release rate in Faber and Evans [2].

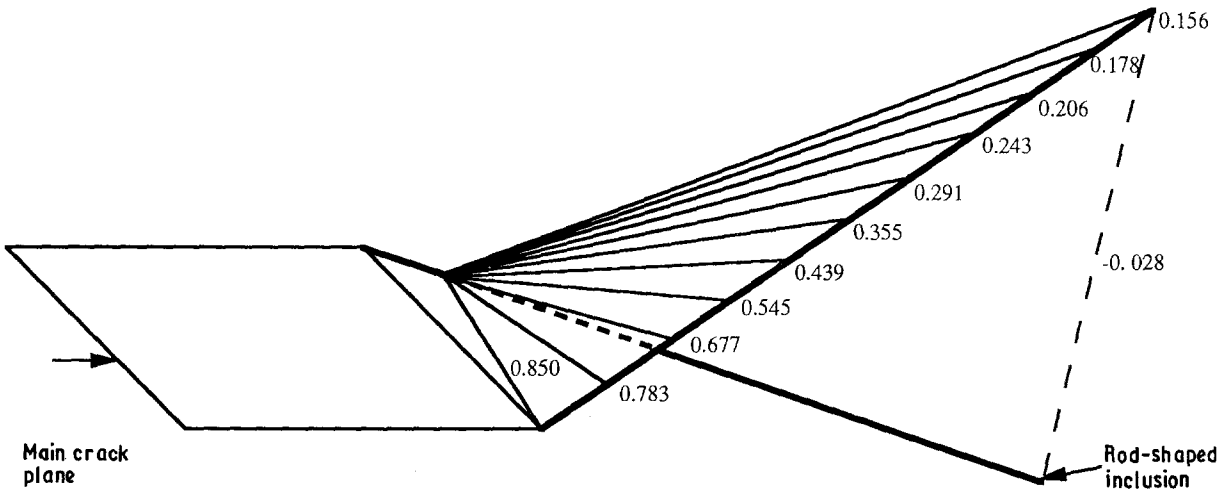

Figure 9 Schematic diagram of the crack paths between two inclusions criss-crossing each other and the relative strain energy release rates, G/G^m, corresponding to the crack front positions for the case of $V_f = 0.2$, $R = 6$, $\alpha = 0.5L$, $\beta = 0.5L$, $\mu_1 = \pi/4$, $\mu_2 = 0$, $\theta_1 = -\pi/6$, $\theta_2 = \pi/3$.

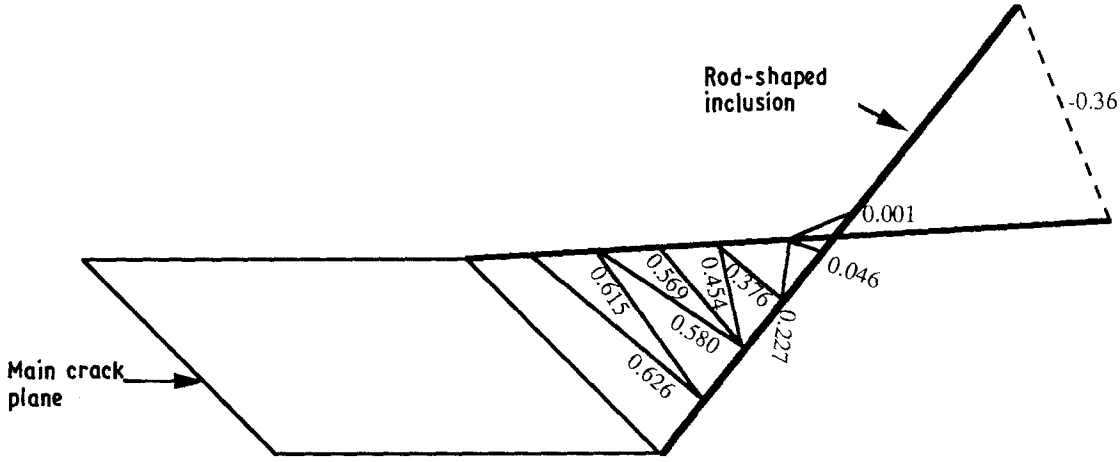

Figure 10 Schematic diagram of the crack paths between two inclusions criss-crossing each other and the relative strain energy release rates, G/G^m, corresponding to the crack front positions for the case of $V_f = 0.2$, $R = 6$, $\alpha = 0.5L$, $\beta = 0.5L$, $\mu_1 = -\pi/4$, $\mu_2 = \pi/4$, $\theta_1 = \pi/6$, $\theta_2 = \pi/3$.

front always reaches the position of the broken line joining the two inclusion ends, and this crack front position is used to calculate the stress intensity factors. It is uncertain whether a crack front will always reach the position indicated by the broken line in Figs 8–10 for the following reasons. First, such a position would be difficult to attain if the difference between the inclusion lengths α and β is significant. Second, the angles μ_1 and μ_2 of the two inclusions could be such that they criss-cross each other in their spatial arrangements. This would require the crack surface to rotate around the inclusions and as a result the strain energy release rate becomes negative, as indicated by the broken lines in Figs 9 and 10. Our calculations have indicated that such crack front configurations are sometimes energetically unfavourable.

The critical strain energy release rates computed from Equations 13 and 2 for the stress intensity factor approach and the crack surface approximation from Equation 19 are the presented in Fig. 11 as a function of inclusion volume fraction. The theoretical predictions of Faber and Evans [2] are also illustrated in Fig. 11. For the stress intensity factor approach the predicted

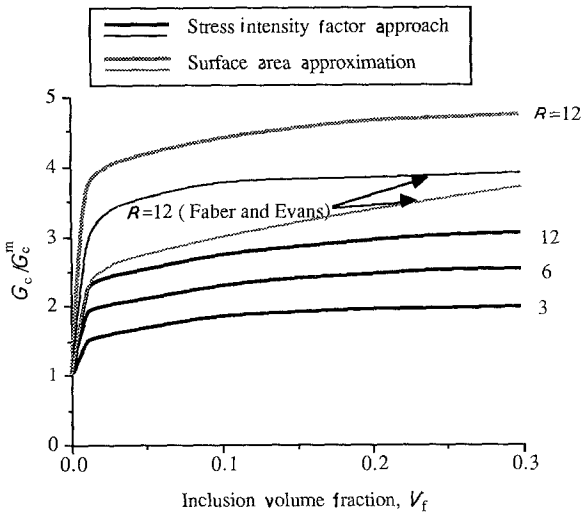

Figure 11 Relative critical strain energy release rate versus inclusion volume fraction.

critical strain energy release rates of the present analysis are smaller than those of Faber and Evans [2]. The difference of the results can be illustrated clearly by Figs 8–10. The relative critical strain energy release

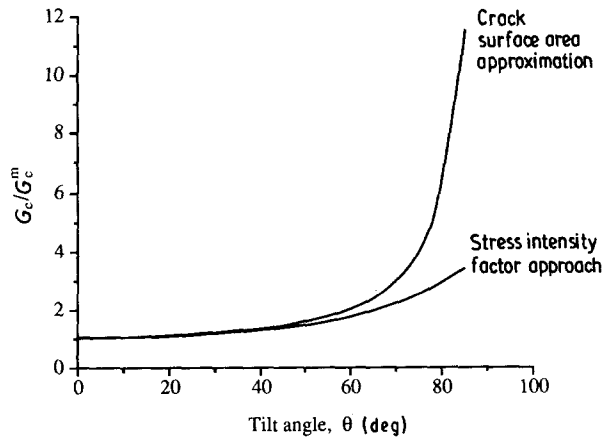

Figure 12 Comparison of relative critical strain energy release rate predictions from the stress intensity factor approach and the surface area approximation for the pure tilt crack (Fig. 1).

rate obtained from Equation 19 based upon a crack surface area approximation is larger than that by the stress intensity factor approach. This phenomenon can be illustrated by the case of pure tilted crack (Fig. 1) as shown in Fig. 12. The crack surface area method gives a close estimation of the critical strain energy release rate for small tilt angles. However, at large tilt angles the crack surface approximation overestimates the increase in the critical strain energy release rate. On the other hand, in the analysis of Faber and Evans [2] the predictions based upon the crack surface area approximation are lower than those by the stress intensity factor approach.

4. Conclusions

The three-dimensional stress intensity factor solutions for deflected cracks have been derived. These formulae can be used to calculate the strain energy release rates of cracks of arbitrary configuration and therefore eliminate the need to use different formulae for evaluating the same-sign and opposite-sign deflections, as defined by Faber and Evans [2]. Because of the use of separate formulae, Faber and Evans's model predicts different results from the same-sign and opposite-sign formulae for the crack configuration where one of the tilt angles vanishes. The present model does not create such inconsistency.

The crack path along two neighbouring rod-shaped inclusions has been identified. In the present analysis, the crack extension along inclusions is governed by the criterion that the crack front seeks to maximize the strain energy release rate. The results show that the assumption of a specific crack front position for achieving maximum toughening is not always appropriate. The knowledge of the crack path is essential for analysing the toughening effect.

Appendix: Local stress intensity factors of a deflected crack

The method for deriving the formulae for the local stress intensity factors of a deflected crack in the present analysis is the same as that of Lawn and Wilshaw [9] in which the stresses acting on the tilted or twisted plane are determined from the stresses at the tip of the undeflected crack by an appropriate tensor transformation. For a tilted crack subject to Mode I loading, the stress intensity factors derived by this method are the same as the first-order solutions by Cotterell and Rice [11] using perturbation procedures. These solutions are almost equivalent to the those of Lo [12] and Kageyama and Chou [13], in which the crack is modelled as a continuous distribution of dislocations.

The local stress intensity of a crack, which is deflected by a tilt angle θ, a twist angle φ and a bias angle ψ (Fig. 3), is evaluated by resolving the components of applied stress into the deflected plane. First, consider a main crack under Mode I loading (σ_y); the corresponding stress intensity factor is denoted as K_I. When the crack is tilted by an angle θ ($\phi = \psi = 0$ in Fig. 1), the stress intensity factors, K_i^t, can be expressed in the following general forms

$$K_I^t = f_1(\theta) K_I \quad \text{(A1)}$$

$$K_{II}^t = f_2(\theta) K_I \quad \text{(A2)}$$

The solutions of $f_1(\theta)$ and $f_2(\theta)$ are given by

$$f_1(\theta) = \cos^3(\theta/2) \quad \text{(A3)}$$

$$f_2(\theta) = \sin(\theta/2)\cos^2(\theta/2) \quad \text{(A4)}$$

The stress components of a cubic element at a distance r from the crack-tip (Fig. A1a), for the plane strain condition, associated with K_I^t are (see for instance Lawn and Wilshaw [9])

$$\sigma_r = \sigma_\theta = \frac{K_I^t}{(2\pi r)^{1/2}} \quad \text{(A5a)}$$

$$\sigma_z = \frac{2\nu K_I^t}{(2\pi r)^{1/2}} \quad \text{(A5b)}$$

$$\tau_{r\theta} = \tau_{rz} = \tau_{\theta z} = 0 \quad \text{(A5c)}$$

where ν is Poisson's ratio. Similarly, the stress components associated with K_{II}^t are

$$\tau_{r\theta} = \frac{K_{II}^t}{(2\pi r)^{1/2}} \quad \text{(A6a)}$$

$$\sigma_r = \sigma_\theta = \sigma_z = \tau_{rz} = \tau_{\theta z} = 0 \quad \text{(A6b)}$$

Fig. A1b shows the original tilted crack plane GHIJ. Now consider a rotation φ of the plane with respect to the r-axis; the resulting crack plane is denoted by EFGH with the coordinate system $r'\theta'z'$. The stress components on the plane EFGH can be easily calculated from the transformation equations. The components that are relevant to the present analysis are

$$\sigma_{\theta'} = (\cos^2\phi + 2\nu\sin^2\phi)\frac{K_I^t}{(2\pi r)^{1/2}} \quad \text{(A7a)}$$

$$\tau_{r'\theta'} = \cos\phi \frac{K_{II}^t}{(2\pi r)^{1/2}} \quad \text{(A7b)}$$

$$\tau_{z'\theta'} = -(1 - 2\nu)\sin\phi\cos\phi \frac{K_I^t}{(2\pi r)^{1/2}} \quad \text{(A7c)}$$

Finally, the bias angle of the crack front is achieved

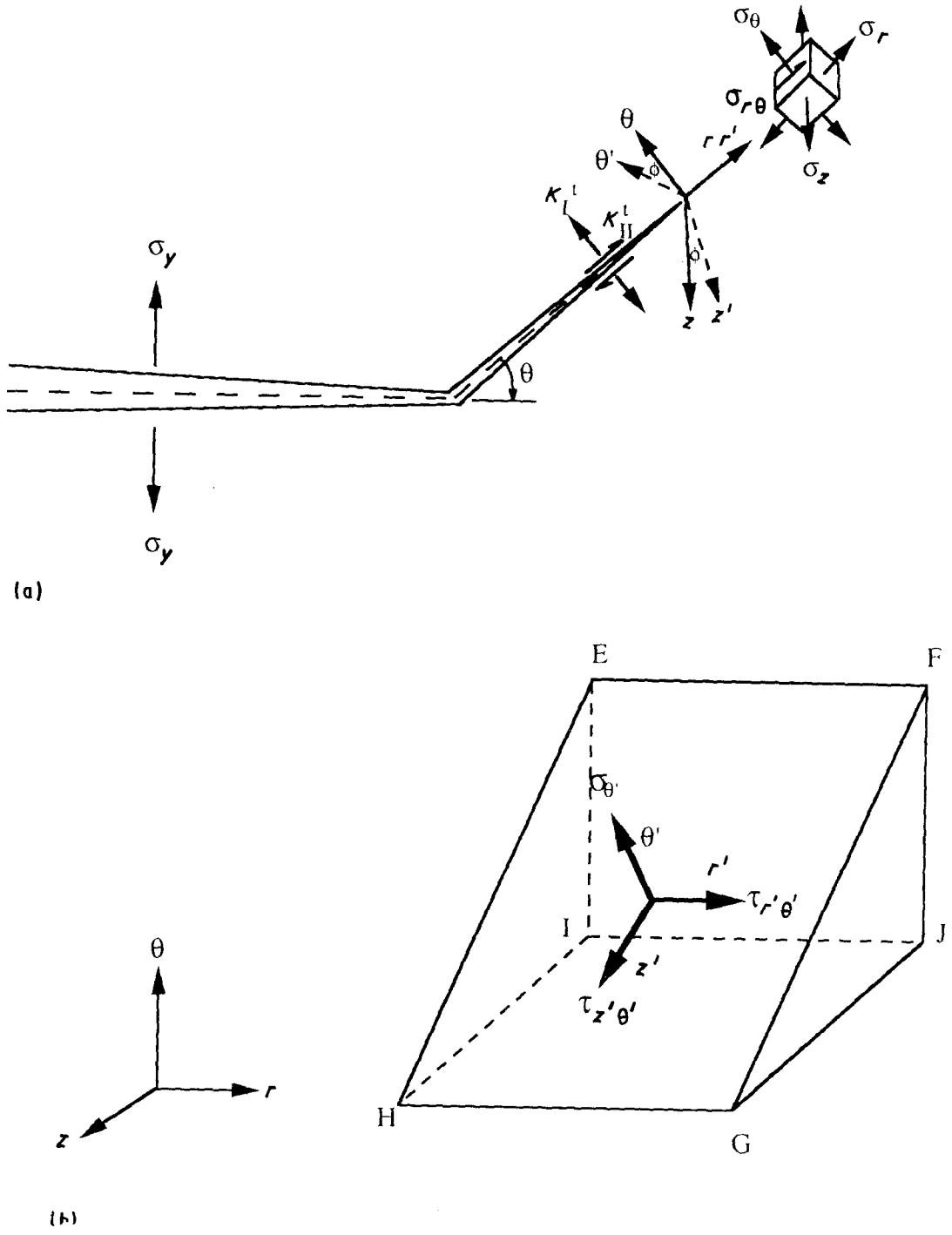

Figure A1 (a) Schematic diagram of the stress components of a cubic element at a distance r from the crack-tip. (b) Schematic diagram of the stress components $\sigma_{\theta'}$, $\tau_{r'\theta'}$ and $\tau_{z'\theta'}$ on the plane EFGH due to the rotation of the θz plane about the r axis by the angle ϕ.

through a rotation by an angle ψ with respect to the θ' axis. The resulting coordinate system is denoted by $r''\theta''z''$. The stress components associated with the fully deflected crack defined by the angles θ, ϕ and ψ can again be found from simple stress transformation relations and Equations A7. The stress components relevant to the subsequent analysis are

$$\sigma_{\theta''} = \sigma_{\theta'} = (\cos^2\phi + 2\nu\sin^2\phi)\frac{K_I^t}{(2\pi r)^{1/2}} \quad \text{(A8a)}$$

$$\tau_{r''\theta''} = \cos\phi\cos\psi\frac{K_{II}^t}{(2\pi r)^{1/2}} - (1 - 2\nu)\sin\phi\cos\phi\sin\psi\frac{K_I^t}{(2\pi r)^{1/2}} \quad \text{(A8b)}$$

$$\tau_{z''\theta''} = -\cos\phi\sin\psi\frac{K_{II}^t}{(2\pi r)^{1/2}} - (1 - 2\nu)\sin\phi\cos\phi\cos\psi\frac{K_I^t}{(2\pi r)^{1/2}} \quad \text{(A8c)}$$

The above results can be presented in the condensed form for the stress field at the tip of a deflected crack front as shown in Equations 3 and 4.

Acknowledgement

The author thanks Dr T. W. Chou for very helpful discussions. This work was supported by the Air Force Office of Scientific Research (Contract No. AFOSR-87-0383). Dr Liselotte J. Schioler is the Program Manager.

References

1. M. GELL and E. SMITH, *Acta Metall.* **15** (1967) 253.
2. K. T. FABER and A. G. EVANS, *ibid.* **31** (1983) 565.
3. *Idem, ibid.* **31** (1983) 577.
4. K. P. GADKAREE and K. CHYUNG, *Amer. Ceram. Soc. Bull.* **65** (1986) 370.
5. N. CLAUSSEN, K. L. WEISSKOPF and M. RUHLE, in "Fracture Mechanics of Ceramics", Vol. 7 (Plenum, New York, 1986) pp. 75–86.
6. P. F. BECHER, T. N. TIEGS, J. C. OGLE and W. H. WARWICK, *ibid.* pp. 61–73.
7. E. TANI, S. UMEBAYASHI, K. KISHI, K. KOBAYASHI and M. NISHIJIMA, *Amer. Ceram. Soc. Bull.* **65** (1986) 1311.
8. C. W. LI and J. YAMANIS, *Ceram. Engng Sci. Proc.* **10** (7–8) (1989).
9. B. R. LAWN and T. R. WILSHAW, "Fracture of Brittle Solids" (Cambridge University Press, Cambridge, 1975).
10. P. P. BANSAL and A. J. ARDELL, *Metallography* **5** (1972) 97.
11. B. COTTERELL and J. R. RICE, *Int. J. Fracture* **16** (1980) 155.
12. K. K. LO, *J. Appl. Mech.* **45** (1978) 797.
13. K. KAGEYAMA and T. W. CHOU, *Int. J. Fracture* in press.

Received 23 July 1990
and accepted 6 February 1991